BRAIN COMMUNICATIONS

Phagocytic glioblastoma-associated microglia and macrophages populate invading pseudopalisades

Elena Saavedra-López,[1] Meritxell Roig-Martínez,[1] George P. Cribaro,[1] Paola V. Casanova,[1] José M. Gallego,[2] Ana Pérez-Vallés[3] and (iD)Carlos Barcia[1]

Hypoxic pseudopalisades are a pathological hallmark of human glioblastoma, which is linked to tumour malignancy and aggressiveness. Yet, their function and role in the tumour development have scarcely been explored. It is thought that pseudopalisades are formed by malignant cells escaping from the hypoxic environment, although evidence of the immune component of pseudopalisades has been elusive. In the present work, we analyse the immunological constituent of hypoxic pseudopalisades using high-resolution three-dimensional confocal imaging in tissue blocks from excised tumours of glioblastoma patients and mimic the hypoxic gradient in microfluidic platforms *in vitro* to understand the cellular motility. We visualize that glioblastoma-associated microglia and macrophages abundantly populate pseudopalisades, displaying an elongated kinetic morphology across the pseudopalisades, and are oriented towards the necrotic focus. *In vitro* experiments demonstrate that under hypoxic gradient, microglia show a particular motile behaviour characterized by the increase of cellular persistence in contrast with glioma cells. Importantly, we show that glioblastoma-associated microglia and macrophages utilize fibres of glioma cells as a haptotactic cue to navigate along the anisotropic structure of the pseudopalisades and display a high phagocytic activity at the necrotic border of the pseudopalisades. In this study, we demonstrate that glioblastoma-associated microglia and macrophages are the main immune cells of pseudopalisades in glioblastoma, travelling to necrotic areas to clear the resulting components of the prothrombotic milieu, suggesting that the scavenging features of glioblastoma-associated microglia and macrophages at the pseudopalisades serve as an essential counterpart for glioma cell invasion.

1 Neuroimmunity Research Group, Department of Biochemistry and Molecular Biology, School of Medicine, Institut de Neurociències, Universitat Autònoma de Barcelona, Bellaterra, Cerdanyola del Vallès, Barcelona 08193, Spain
2 Department of Neurosurgery, Valencia General Hospital, Valencia 46014, Spain
3 Department of Pathology, Valencia General Hospital, Valencia 46014, Spain

Correspondence to: Carlos Barcia, PhD, Neuroimmunity Research Group, Department of
Biochemistry and Molecular Biology, School of Medicine, Institut de Neurociències, Lab M2-107,
Universitat Autònoma de Barcelona, Bellaterra, Cerdanyola del Vallès, Barcelona 08193, Spain
E-mail: carlos.barcia@uab.es

Graphical Abstract

Introduction

Pseudopalisades (PP)-s are one of the critical pathological features of glioblastoma (GBM; Brat and Van Meir, 2004; Rong *et al.*, 2006). They are densely populated layers of cells, surrounding certain necrotic areas of the tumour (Wippold *et al.*, 2006). Their origin and function are still debated but they are considered as a canonical GBM diagnostic feature for neuropathologists, as well as an indicator of high malignancy and invasive capacity. Previous studies have described PPs as a population of tumour cells that escape from the necrotic and hypoxic foci to form rather organized structures (Brat and Van Meir, 2004; Brat *et al.*, 2004). However, despite the advances in GBM research, the cause and implications of PPs in brain tumours still remain mysterious. Importantly, these strata of gathered cells are orderly disposed around necrotic foci (NF), geographically associated with a central blood vessel (BV), which appears to be occluded upstream by factors derived from the tumour cells and probably by the tumour mass development itself (Rong *et al.*, 2006). It is thought that the lack of oxygen and probably low glucose levels cause massive cell death in these areas. A circumstance that creates a hypoxic milieu where tumour malignant cells escape from, in a centrifugal way, forming these aligned structures. The cells building up PPs are placed in very close apposition to each other, delimiting necrotic tissue and probably containing this adverse environment. Considering the active cell death process within these areas, and the high quantity of cellular debris, it would be expected to be associated with a robust inflammatory response. However, the most cited and comprehensive study of PPs to date, reported very limited, if any, amount of inflammatory cells in these arranged structures (Brat *et al.*, 2004).

In the present work, we revisited and studied the neuroinflammatory compound of PPs in human GBM specimens, and we attempted to understand its function in this tumour microenvironment. We particularly focused on studying GBM-associated microglia and macrophages (GAMMs) because they are a predominant immune-cell population in this type of brain tumour (Poon *et al.*, 2017), and most importantly, because it is established that GAMMs predominantly have a pro-tumoural influence (Hambardzumyan *et al.*, 2016). However, the machinery by which they contribute to the invasive features of GBM is still poorly understood.

We observed that a large population of GAMMs coexist as a big part of the cellular structure of GBMs' PPs. Experiments with cell culture microfluidic platforms show that microglial cells are highly motile compared with glioma cells and show particular dynamics when exposed to a hypoxic gradient, consistent with the migrating features observed in PPs. Detailed study of kinetic microglia under hypoxia revealed the preferential orientation of the microtubule-organizing centre (MTOC) towards the cells' leading edge. This feature was then analysed in GAMMs in the PPs of human biopsies, demonstrating the centripetal and anisotropic tendency of these cells towards the NF. Finally, three-dimensional (3D) reconstructions and transparencies of tissue blocks revealed the haptotactic interaction of GAMMs with fibrous tumour cells and the increased phagocytic capacity of migrating GAMMs in the internal limit of the PPs. With this study, we demonstrate that a large proportion of the cellular component of PPs is microglia and macrophages, having a significant implication for the dynamics of glioma.

These findings, unascertained until now, challenge previous knowledge describing a barely existent immune component in this GBM hallmark and indicate that

GAMMs migration and debris clearance in this tumour location is essential for glioma cell invasion.

Material and methods

Human tissue studies

Patients and samples

For this research, we selected biopsies from six patients from a cohort of samples of the General Hospital of Valencia diagnosed with GBM containing evident necrotic PPs. Before surgery, the patients presented the classical GBM physiopathology and symptomatology, with the expected clinical evolution and the confirmation of the tumour presence by neuroimaging. Tumour excision was performed at the surgery room and biopsies were handled with minimal manipulation. Part of each sample was used for routine neuro-pathological examinations and diagnosis, while the samples used from this study came from 2.5 ml of the tissue, which were submerged during 1 week in 4% paraformaldehyde before being washed with phosphate-buffered saline (PBS) 0.1 M/l, pH 7.4 and stored in PBS with 0.1% sodium azide until being sectioned by vibratome (Leica Microsystems, Germany) into 60 μm slices. The study was performed with the approval of both institutions involved and in compliance with the 1964 Declaration of Helsinki, including the informed consent of the patients. The excised tumour had the typical GBM pathological features, such as high glial fibrillary acidic protein (GFAP) and Vimentin reactivity, as well as Ki-67 expression, and showed different layers of the tumour, from the peripheral healthy-like tissue to the necrotic core. Besides the clear presence of PPs, all tumours showed hyperchromatism and pleomorphism, with marked cellularity, glomeruloid vessels, gemistocytic formations and aberrant mitoses.

Histochemistry

Thionine staining was performed to analyse the anatomical structure of the tissue, detect the nuclei of the cells and visualize the cell-division status of each tumour. For each sample, we were able to see the classical GBM histopathological features, including the presence of PPs (Fig. 1). For this, thionine (acetate; Certistain; Merck KGaA; Darmstadt, Germany) solution (25 mg/100 ml acetate buffer pH: 4.6) in acetate buffer solution (Stem solution A, sodium acetate 0.1 M; Stem solution B, Acetic acid 0.1 M) was used. All the samples were first mounted on gelatinized slides, dried and then rinsed in distilled water, stained in thionine solution for 5 min, washed in distilled water, dehydrated in increasing concentrations of ethanol and Xylene. Then, sections were cover-slipped to be analysed at the conventional light microscope (Eclipse 80i microscope, Nikon), taking the required pictures with a digital camera connected to the microscope (DXM 1200F Digital Camera, Nikon).

Immunohistochemistry

Free-floating immunohistochemistry by diaminobenzidine detection was performed on tumour sections to visualize immune-cell markers and glial-tumour-cell markers. In order to identify GAMMs, antibodies against antigens commonly expressed by macrophages were used. Anti-inflammatory macrophages were identified by positive immunostaining of the cell-surface marker Cluster of Differentiation 163 (CD163), whereas the panmacrophage/microglia marker used was Ionized calcium-binding adapter molecule 1 (Iba-1; also named AIF-1). Human leucocyte antigen (HLA)-DP, -DQ, -DR (major histocompatibility complex II or MHCII) was also used to see the myeloid cell population within the pro-inflammatory spectrum. Specifically, primary antibodies used were those to recognize: Iba-1 (1:500, polyclonal rabbit immunoglobulin (Ig) G; Wako Pure Chemical Industries, Ltd.; Osaka, Japan); CD163 (1:150, monoclonal mouse IgG; Abcam; Cambridge, UK); and MHCII (1:100, mouse IgG1; Dako Cytomation; Glostrup, Denmark). Samples were first treated with citrate (10 mM, pH 6, 60°C, 20 min) to ameliorate antibody binding by antigen retrieval. At that point, 0.3% hydrogen peroxide was used to block endogenous peroxidase, and sections were blocked for 1 h with 0.5% Triton X-100 with 10% horse serum (HS10%; Sigma-Aldrich; St. Louis, MO, USA) before incubating overnight with primary antibody diluted in Trizma Base Saline (TBS)-0.5% Triton X-100, 1% horse serum and 0.1% sodium azide. The primary antibodies used are described above. Secondary antibodies were biotinylated goat anti-mouse or biotinylated goat anti-rabbit (1:1000, goat; Dako; Denmark), diluted in 0.5% Triton X-100 with 1% horse serum and 0.1% sodium azide, accordingly to the host of the primary antibodies. Secondary antibodies were detected by the Vectastain Elite ABC horseradish peroxidase method (Vector Laboratories; CA, USA). Sections were mounted on gelatinized glass slides and were dehydrated through graded ethanol solutions (70%, 80%, 90% and 100%) and submerged in Xylene before coverslipping. The sections were then analysed at the microscope (Eclipse 80i microscope, Nikon), taking the required pictures with a digital camera connected to the microscope (DXM 1200F Digital Camera, Nikon).

Immunohistofluorescence

Free-floating immunofluorescence was performed on tumour sections for multiple stainings to visualize Iba-1$^+$ cells with their MTOC or combined to also see GFAP$^+$ cells and the cells' relation to BV. Antigen retrieval and blocking were done as previously mentioned before incubating during 48 h with the primary antibodies diluted in 1% HS. The primary antibodies used were anti-human Iba-1 as described for the immunohistochemistry (1:500, rabbit polyclonal; Dako Cytomation; Glostrup, Denmark); anti-MHCII (1:100, mouse IgG1; Dako Cytomation; Glostrup, Denmark); anti-GFAP (1:500, chicken IgY; Abcam, Cambridge, UK); anti-γ-tubulin (to
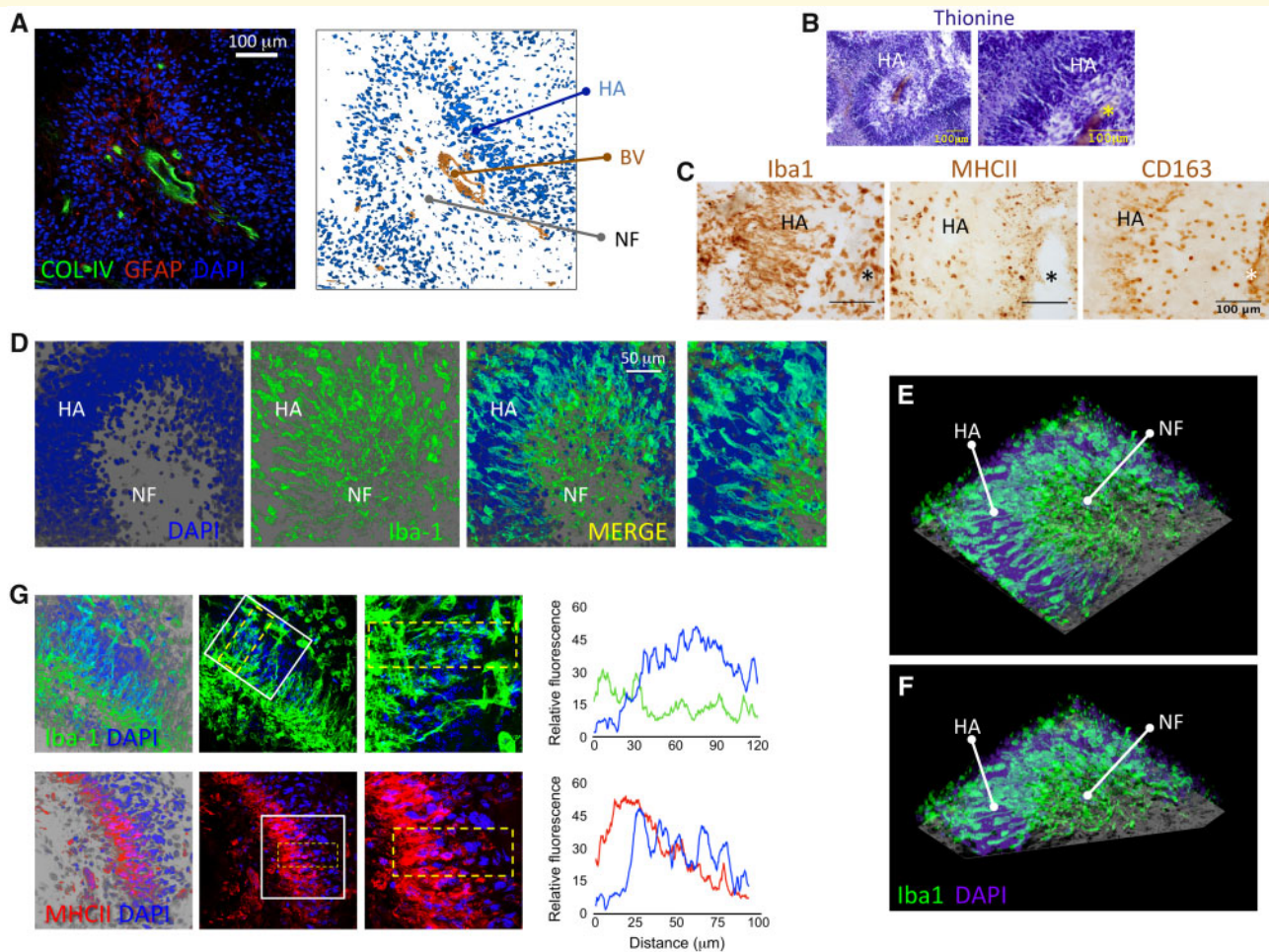
Figure 1 GAMMs constitutively form PPs in GBM. (A) Confocal image and diagram of a classic PPs structure, containing HA, central BV and NF. [Diagram based on confocal image with characteristic architecture of a PP. BV identified by COL-IV (green) is located at the centre of the NF. Malignant tumour cells and remaining astrocytes, identified by GFAP (red) appear in a centrifuging manner, escaping from the necrotic areas (as previously described by Brat *et al.*, 2004). A clear accumulation of DAPI$^+$ nuclei (blue) can be appreciated forming the palisade arrangement]. **(B)** Thionine-based Nissl staining evidences necrotic PPs in GBM samples. **(C)** Adjacent histological sections of the HA show a dense population of elongated Iba-1$^+$ GAMMs, with a scarce frequency of the pro-inflammatory spectrum (MHCII), and expression of the anti-inflammatory spectrum (CD163$^+$) delineating the HA (asterisk indicates the central BV). **(D)** Confocal transparency shows that the area of high density of DAPI$^+$ nuclei (blue) (HA) is densely populated by Iba-1$^+$ GAMMs. **(E)** 3D reconstruction of the PP (shown in D) displays elongated Iba-1 cells at the HA. **(F)** Three-dimensional reconstruction from E with a central clipping plane to visualize elongated cells at the HA. **(G)** Confocal transparencies show the distribution of Iba-1 (top panel) and MHCII (bottom panel) within the HA. Measurements of the relative fluorescence are shown in the plots obtained from the region of interest (yellow broken line) at the HA. MHCII is notably increased at the NF whereas Iba-1 expression is steady along the HA.

detect the MTOC; 1:500, mouse IgG1; Sigma-Aldrich; Saint Louis, MO, USA); anti-CD31 (1:200, mouse monoclonal IgG1; Abcam, Cambridge, UK); anti-collagen IV (COL-IV; 1:200, rabbit polyclonal; Abcam, Cambridge, UK); and anti-CD3 (1:100; rabbit polyclonal; Dako Cytomation; Glostrup, Denmark). Secondary fluorescent antibodies diluted in 1% HS were used accordingly with the host of the primary antibodies. For the study of the cells' directionality, we used AlexaFluor 488 Goat anti-rabbit 1:1000 (Life Technologies; Carlsbad, CA, USA; also used to detect anti-COL-IV) and AlexaFluor 555 Goat anti-mouse IgG1 1:1000 (Life Technologies;

Carlsbad, CA, USA; likewise for CD31); and on the other hand, 488 Goat anti-rabbit 1:1000 (Life Technologies; Carlsbad, CA, USA) and AlexaFluor 555 Goat anti-Chicken 1:500 (Life Technologies; Carlsbad, CA, USA) to see the cells' interactions. When staining CD3, the secondary antibody used was AlexaFluor 647 Goat anti-rabbit 1:1000 (Life Technologies; Carlsbad, CA, USA). Then 4′,6-diamino-2-phenylindole (DAPI; 1:1000; Life Technologies; Carlsbad, CA, USA) was used to stain the nuclei of the cells. Sections were mounted on glass slides and cover-slipped using Prolong antifade reagent (Invitrogen; Carlsbad, CA, USA).

Confocal microscopy, 3D analysis and quantification

Human biopsies stained by immunofluorescence were imaged with a confocal laser-scanning microscope (LSM 700, Carl Zeiss, Oberkochen, Germany) utilizing a Plan-Apochromat 40×/1, 3 Oil DIC M27 objective lens (Carl Zeiss) and processed with the ZEN 2010 software (Carl Zeiss). Three-dimensional reconstructions were generated using the α blending softwares ZEN 2010, Imaris (BitPlane, South Windsor, USA) and iLlucida FX (iLlucida LLC, Los Angeles, USA) as we recently described (Diaz et al., 2018). Z-stacks in the regions of interest were acquired to cover the depth of the tissue (25–30 images/ stack) with a 0.5-μm-step size, and the images for quantification were always taken with the NF on the upper part of the image, considering that the scanning field could be rotated and oriented. Raw images were imported into both Imaris (Bitplane Zurich, Switzerland) and Image J (version 1.4.3.67, NIH, USA) softwares, where they were further processed for morphometric analyses and cell counts. For the cells' directionality, in order to better visualize the MTOC, zoom 1.7× was used, while the Iba-1/ GFAP staining was visualized with zoom at 1.0×. On the former, the Iba-1 channel composing the Z-stack was iso-surfaced using Imaris Surpass, in order to view a 3D representation of the Iba-1$^+$ cells. To detect the MTOC within the cells, the module Spots was used. Within the cell module, the nuclei were detected and then the MTOCs were imported with the Vesicles tool. The Iba-1 surfaces were imported as the cells' cytoplasms. This way α blending software Imaris, (Bitplane, Zurich, Switzerland) and iLlucida FX (iLlucida LLC, Los Angeles) allowed the free rotation of the 3D reconstructions of 23 images from all tumours, which were analysed to see Iba-1$^+$ cells' directionality by the observation of the distribution of the MTOC of interest within the cells. The same procedure was performed when analysing the cells' diameter and perimeter at the different positions within the PPs. This time, seven PPs were divided into three regions, which we called "proximal" (P), "intermediate" (I) or "distal" (D), corresponding to the relative distance of the zones to the NF as illustrated in descriptive diagrams (Fig. 2). The criteria for this regionalization were established by the following defined steps: once a PP was identified, the internal and external limits of the hyper-cellular area (HA) were set according to the position of the NF. Then, an equidistant distribution of the three regions of interest (P, I and D) was established according to these limits. As indicated above, the confocal sampling was made allowing the rotation of the scanning head, always positioning the NF on the upper part of the image (Fig. 2). This rotation allowed the analysis of the orientation of GAMMs in 3D reconstructions. Further morphometric studies were performed on single stereological dissectors of confocal images of eight PPs, either in the HA or the NF, and by means of image analysis software (Image J), we analysed the Area, Aspect Ratio, Roundness and Circularity of cells in these two areas.

In the case of the Iba-1/GFAP staining, a grid was drawn on the image with Image J software on 23 palisade images from five tumours. This grid was made of nine centred 1600 μm^2 squares, which determined three areas, which we again called P, I and D, corresponding to the relative distance of the zones to the NF. Of the nine squares, only the central column was taken into account, and only one central slice of each palisade was analysed to obtain the values of the number of nuclei, the different types of phagocytic events and the kind of intercellular contacts (longitudinal or perpendicular), which were then extrapolated in order to obtain values per mm^2. The percentage of Iba1$^+$ cells was then compared in the HA and in the tumour parenchyma (TP). The TP images were taken in the same samples and with the same conditions, and equally a grid of 1600 μm^2 squares was established for stereological purposes. To see the number of contacts in general, by means of the ImageJ software, a cross grid with an area of 800 μm^2 per point was drawn. An intermediate optical slice of each Z-scan per palisade was chosen, and Iba-1$^+$ cells hitting the crosses were analysed to see the number of contacts with GFAP$^+$ cells in the depth of the z-stack. This way we were able to determine the contacts between Iba-1$^+$ cells and GFAP$^+$ material in the different areas of the palisade, as two rows of crosses corresponded to each of the 'P', 'I' or 'D' zones, as we resolved before.

Cell culture studies

Cell culture and treatment

BV2 (murine microglia), HAPI (rat microglia; both obtained from the Cell Cultures unit at the *Institut de Neurociències*) and GL261 (murine glioma; purchased from the National Cancer Institute at Frederick) were maintained in RPMI-1640 medium (Sigma-Aldrich, Saint Louis, MO) supplemented with 10% heat-inactivated foetal bovine serum, 0.1% penicillin/streptomycin at 37°C and 5% CO_2 in a humidified incubator. C6 (rat glioma; Obtained from Culture Collections, Public Health England, Salisbury, UK) was maintained in F12 medium (Sigma-Aldrich, Saint Louis, MO) supplemented with 5% foetal bovine serum, 0.1% penicillin/streptomycin at 37°C and 5% CO_2 likewise in a humidified incubator. In order to do immunostainings, cells were seeded on coverslips pre-treated with poly-L-lysine at a concentration of 25 μg/ml and washed twice with PBS.

In regard to seeing how glucose deprivation affected cells, murine microglia and glioma cell lines were seeded into 24-well culture plates 1 day before treatment at a density of 50 000 cells/ml, and the day of the experiment the medium was changed for fresh medium, either glucose-free RPMI-1640 supplemented with 0.1% penicillin/ streptomycin, or the same medium but also supplemented with L-glucose at a final concentration of 2 g/l. After 24 h, cells were fixed with 4% paraformaldehyde before immunostaining.
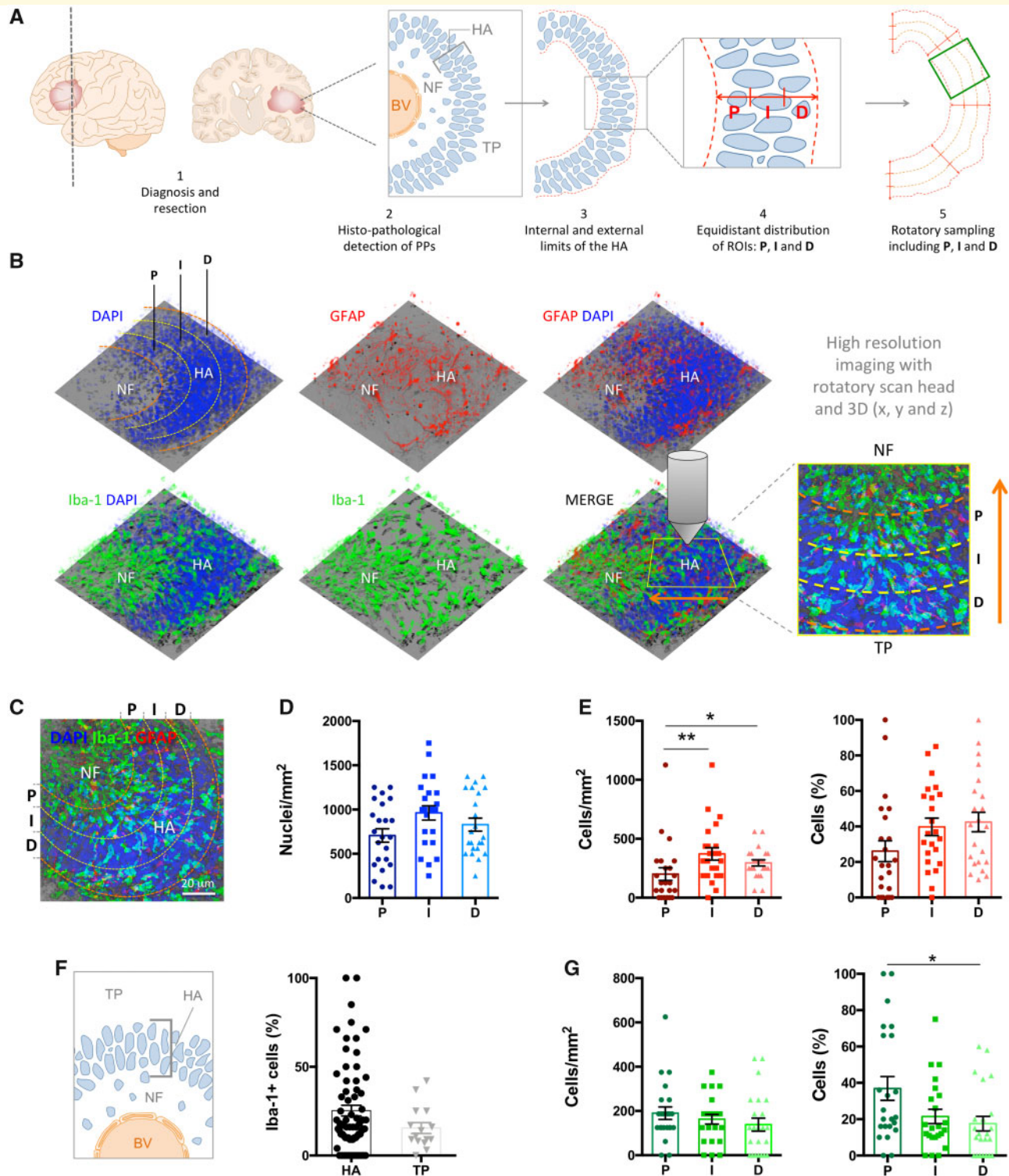
Figure 2 Differential distribution of GAMM and tumour cells within PPs. (**A**) Diagram illustrating the criteria utilized for the classification of the HA in proximal (P), intermediate (I) and distal (D) regions. (**B**) The 3D reconstructions of a representative human tissue block at a PP containing the NF and HA, which was divided in P, I and D. High-resolution scanning frames of the HA were captured with rotated orientation comprising P, I and D for quantification considering *x*-, *y*- and *z*-axis. (**C**) Representative zenithal view of the areas of quantification. (**D**) Estimation of nuclei density in the HA of PPs. (**E**) Estimation of GFAP+ nuclei (left) and percentage from the total nuclei (right). (**F**) Quantification of the percentage of Iba-1+ cells in the HA compared with the TP. (**G**) Estimation of Iba-1+ nuclei (left) and percentage from the total nuclei (right).

For the hypoxia experiment, both murine cell lines were seeded into 24-well culture plates 1 day before treatment as previously described, and the day of the experiment the medium was replaced with fresh supplemented RPMI-1640 medium and cells were incubated in either the humidified incubator with normoxic (21% oxygen) conditions, in the same conditions with $CoCl_2$ (100 μM) as a positive control for hypoxia; or in the hypoxic (Baker Ruskinn InvivO$_2$ 200) workstation, always at 37°C and 5% CO_2. After 24 h, cells were fixed with 4% paraformaldehyde before immunostaining.

Microfluidic plates (CellASIC^{TM} ONIX M04G-02-5PK, EMD Millipore Corporation; Hayward, CA, USA) were used to record the natural movement of BV2 and GL261 cells, thus under normoxic and normoglycemic conditions. For this, after treating the plate with poly-L-lisine (25 μg/ml) and washing it, cells were plated at a low density to avoid confluence during the experiment. After 24 h in the humidified incubator, flows of normally supplemented RPMI-1640 were created, what permitted us to record the cells in an always-fresh medium.

The same microfluidic plates (CellASIC^{TM} ONIX M04S-02, Merck) were also used to see how BV2 and GL261 cells reacted to a hypoxic gradient, simulating pseudopalisades' dynamics, similarly to a recently published system (Ayuso et al., 2017). Hence, after treating the plate with Poly-L-lisine (25 μg/ml) and washing it, cells were plated at a low density to avoid confluence during the experiment. Creating flows of Normoxic RPMI-1640 medium normally supplemented and the same medium but bubbled with N_2 in order to displace the O_2 in it (hypoxic medium), we achieved the creation of a gradient in the chambers where the cells were seeded.

The position of the MTOC was analysed in BV-2, GL261 and HAPI cell lines, as well as primary rat microglia. While the cell lines were seeded as previously described in poly-L-lysine pre-treated coverslips at a concentration of 50 000 cells/ml; primary rat microglial cells were seeded at a concentration of 100 000 cells/ml. For this to be done, newborn Sprague Dawley rats (post-natal days 0–2) were sacrificed in order to obtain the glia from their cortex and/or mesencephalon. The animals were obtained from the animal facility of the *Universitat Autònoma de Barcelona* (UAB), where the experiments were carried out, following the protocol approved by the Ethics Committee on Animal and Human Research of the UAB. Five solutions were used throughout the culture, and all of them were filtered (0.2 μm filter) prior their use: Solution 1 consisted of 50 ml Krebs buffer (120 mM NaCl, 4.8 mM KCl, 1.2 mM KH_2PO_4, 25 mM $NaHCO_3$, 14.3 mM Glucose), with 0.15 g BSA (Sigma-Aldrich, St. Louis, MO, USA) and 0.4 ml $MgSO_4$ 3.8%. Solution 2 was created with 10 m Solution 1 and 2.5 mg trypsin (Sigma-Aldrich, St. Louis, MO, USA). To make Solution 3, 10 ml of Solution 1 were mixed with 0.8 mg DNase (Sigma-Aldrich, St. Louis, MO, USA), 5.2 mg of trypsin

inhibitor (Gibco) and 0.1 ml $MgSO_4$ at 3.8%. Solution 4 consisted of 8.4 ml Solution 1 and 1.6 ml Solution 3. Finally, Solution 5 was a mix of 5 ml Solution 1, 40 μl $MgSO_4$ 3.8% and 6 μl $CaCl_2$ 1.2%. After the whole brain was extracted, the meninges were discarded and the required tissue was separated from the rest of the brain. It was cut in small sections and re-suspended in 15 ml Solution 1. This was followed by centrifugation (30 s, 1500 rpm) and the pellet containing the cells was re-suspended in the Solution 2 and incubated 10 min at 37°C, with gentle mixing every 2–3 min to better digest the tissue. This enzymatic digestion was stopped when adding Solution 4 and everything was centrifuged again at 1500 rpm. The pellet was re-suspended in 3 ml Solution 3 and mechanical disaggregation was performed by gently pipetting up and down with a Pasteur pipette 10 times. The cells were isolated into a uniform single-cell suspension by the use of a cell strainer and gently pipetting again up and down 10 times. All this cell suspension was added to the tube with Solution 3 before centrifuging 5 min at 1000 rpm. Again, the supernatant was discarded and the pellet was re-suspended in 10 ml DMEM supplemented with 1% penicillin/streptomycin and 10% foetal bovine serum, medium in which the cells were later on cultured. After re-suspension, cells were counted to be cultured at the desired density, 300 000 cells/ml, in a culture flask or 24-well plates at 37°C and 5% CO_2. The medium of these cells was partially changed (50%) for fresh medium every week until confluence was achieved. Then, the flasks were shaken at 300 rpm for 2 h in order to extract the microglia and seeded on poly-L-lysine pre-treated coverslips at 100 000 cells/ml.

In order to study the phagocytic capacity of microglial cells, a primary culture of rat cortical microglia was performed like described above. Once the culture reached confluence, the glia was agitated and the cortical microglia extracted was cultured at 100 000 cells/ml in 24-well plates with 50% conditioned media. To activate microglia, interferon gamma (25 ng/ml) and lipopolysaccharide (10 ng/ml) were added. After 24 h, astrocytes from the same rats or early-passage C6 glioma cells were collected by tripsinization and co-cultured with the microglia at also 100 000 cells/ml for 2.5 h before cell culture fixation. To detect C6 glioma cells in the co-culture, cells were previously centrifuged (1500 rpm, 2 min) and re-suspended in PBS to be stained with CellMask^{TM} Deep Red Plasma Membrane stain (1:1000, ThermoFisher Scientific), for 15′ at 37°C, before dilution to 100 000 cells/ml in their medium. Alternatively, GFAP immunocytofluorescence was also performed in the co-cultures as described in the following section.

Immunocytofluorescence

The cells were stained to analyse their morphology. After cell fixation, paraformaldehyde was washed with PBS and cells were treated for antigen retrieval with PBS with 0.02% saponine for 7 min. After washing this solution, a

mild blocking solution was added (PBS with 0.01% saponine, 10 mM glycine) for 15 min before blocking with a more concentrated solution for 1 h (PBS with 0.01% saponine, 10 mM glycine, 5% BSA). The primary antibody anti-γ-tubulin (1:500, mouse IgG1; Dako Cytomation; Glostrup, Denmark) was diluted in PBS with 0.01% saponine, 1% BSA, and left in a humidity chamber overnight at 4°C. AlexaFluor 555 Goat anti-mouse IgG1 1:1000 (Life Technologies; Carlsbad, CA, USA) was used as a secondary antibody for 45 min, and after washing, Alexa Fluor 647 Phalloidin (Life Technologies; Carlsbad, CA, USA) was used for the analysis of the protrusions and Alexa Fluor 488 Phalloidin (Life Technologies; Carlsbad, CA, USA) was used for the morphometric analyses, both at 1:40 for another 45 min. In the case of the co-cultures, primary rat microglia and C6 rat glioma cells were stained to visualize the phagocytic capacity. After cell fixation, paraformaldehyde was washed with PBS and cells were treated for antigen retrieval with PBS with 0.02% saponine for 7 min. After washing this solution, a mild blocking solution was added (PBS with 0.01% saponine, 10 mM glycine) for 15 min before blocking with a more concentrated solution for 1 h (PBS with 0.01% Saponine, 10 mM glycine, 5% BSA). The primary antibodies used were: anti Iba-1 (1:500, rabbit IgG; Wako, Osaka Japan) or anti- OX42 (1:500, mouse IgG2a; Abcam; Cambridge, UK) to stain the microglial cells and anti-GFAP (1:500, chicken IgY; Abcam, Cambridge, UK) for C6 and astrocytes. They were diluted in PBS with 0.01% Saponine, 1% BSA and left in a humidity chamber overnight at 4°C. AlexaFluor 488 Goat anti-rabbit IgG 1:1000 (Life Technologies; Carlsbad, CA, USA) was used as a secondary antibody to detect Iba-1^{+} cells; AlexaFluor 488 Goat anti-mouse IgG2a 1:1000 (Life Technologies; Carlsbad, CA, USA) was used as a secondary antibody to detect OX42^{+} cells; while AlexaFluor 555 anti-chicken 1:500 (Life Technologies; Carlsbad, CA, USA) to see C6 cells and astrocytes. The secondary antibodies were incubated for 45 min. Nuclei were counterstained with DAPI for 5 min before washing with PBS and mounting the coverslips on glass slides using Prolong antifade reagent (Invitrogen; Carlsbad, CA, USA).

Microscopy, analysis and quantification

Cells stained to see their MTOC and actin in 647 were sampled with the confocal laser-scanning microscope (LSM 700, Carl Zeiss) and a Plan-Apochromat 40×/1, 3 Oil DIC M27 objective lens (Carl Zeiss), to be processed with the ZEN 2010 software (Carl Zeiss). Three-dimensional reconstructions were generated using the α blending softwares ZEN 2010, Imaris (BitPlane, South Windsor, CT, USA) and iLlucida FX (iLlucida LLC, Los Angeles, CA, USA). Z-stacks were acquired to cover the entire monolayer of the culture (20–25 images/stack) with a 0.5 μm step size. One picture was taken for each replicate, being done triplicates. Only cells with clear protrusions with an aspect ratio >1.5 were taken into account.

In order to analyse the cells' morphology, all replicates were sampled homogeneously using a fluorescence (Nikon Eclipse 90i) microscope attached to a DXM 1200F digital camera. Pictures were taken at a 20× objective using the software ACT1 version 2.70 (Nikon corporation).

Regarding the cells' kinetic activity, we imaged the cells in the microfluidic plates with an Eclipse TE2000-E inverted microscope, taking pictures at 10× every 15 min for 24 h. Three time-lapse videos per condition were analysed to track the cells in hypoxic gradient, using the Chemotaxis Tool Plugin in ImageJ (version 1.4.3.67, NIH, USA). The analysis of the motility provided the following parameters: directionality, centre of mass, accumulated distance, velocity and Euclidean distance (note: Euclidean distance is defined as the ordinary straight-line distance between two points. Increasing Euclidean distance indicates a straighter displacement, which in cell biology is recognized as cellular persistence).

Statistical analysis

For human tissue, the number of cells in the palisades, the contacts and the phagocytic events were calculated from over 20 3D reconstructed multi-colour z-stacks of the PPs along the tumour samples (total 3D stacks, $n = 23$). The detailed analysis of the cells' directionality, 3D individual cell-reconstructions, iso-surface rendering, morphology and MTOC position within PPs was scrutinized from 59 cells ($n = 59$). *In vitro*, experiments for the study of the MTOC position with respect to the protrusion and the cells' morphology were performed twice, while the time-lapsed cells tracked were 30 cells each experiment ($n = 30$). Student's *T*-test was used for dependent/independent samples and Mann–Whitney *U* test was used to compare data between groups. For instance, the cells' directionality was seen manually, and *T*-tests were performed to see if there was a statistical difference between the number of cells going towards or away from the necroses. The cells' perimeter and diameter in the tumours were given by the Imaris software when selecting individual cells, and the results were submitted to Kruskal–Wallis test with Dunn's multiple comparisons test, as the data did not follow a normal distribution. For the same reason, the number of nuclei, the phagocytic events and the intercellular contacts were submitted to Kruskal–Wallis tests with Dunn's multiple comparisons test. The results of the percentage of Iba1+ cells in the HA and TP, the cells' morphology, as the kinetic differences between BV2 and GL261 lines, were analysed by Student's *T*-test. Cells' persistence when time-lapsed was determined by Rayleigh test, where $P \leq 0.05$ indicated directionality. In all cases, $P \leq 0.05$ was considered significant. Graphs show the mean values obtained ± standard error of the mean. All statistical analyses were performed using Prism 6 software (GraphPad Software),

except the Rayleigh test, which was performed by ImageJ's chemotaxis plugin.

Data availability

All the raw data supporting the results of the present study are available at the reader's request.

Results

GAMMs densely populate PPs in human GBM

We selected GBM samples from a cohort of biopsies obtained from patients that underwent surgery and based on the histological features, we evaluated the presence of canonical PPs in the tissue sections. Necrotic PPs were identified by a HA, well organized and distributed surrounding a NF with a central BV (Fig. 1 and Supplementary Fig. 1). Nuclear staining clearly revealed the HA, accompanied by GFAP immuno-reactive cells demonstrating the presence of malignant cells and remaining reactive astrocytes. Marker for vascular basement membrane, COL-IV, also demonstrated the central position of BV along the 3D organization of PPs (Fig. 1 and Supplementary Fig. 1). Serial sections of the tumours with identifiable PPs were stained for several GAMM markers (Iba-1, CD163 and HLA-DR), as well as for a general marker for T lymphocytes (CD3). Iba-1 and CD163 immunohistochemistry showed cells clearly outlining the PPs at the HA, demonstrating the big proportion of the immune component of the PPs. However, HLA-DR (the human MHCII form) staining did not reveal an evident palisade outline, being patent outside the HA at the PPs borders (Fig. 1C and G). In addition, T cells were only limited to the BV surroundings but absent from the HA of the PPs (Supplementary Fig. 2).

Our transparent 3D reconstructions of the tissue blocks allowed the visualization of elongated GAMMs crossing the HA areas (Fig. 1 D–F and Video 1). Furthermore, we compartmentalized the HA of the PPs in three regions, proximal (P) to the NF: intermediate (I); and distal (D), the latter appearing close to the malignant TP (Fig. 2A–C); and quantified the proportion of Iba-1$^+$ GAMMs and GFAP$^+$ cells (Fig. 2C–G). The percentage of Iba-1$^+$ GAMMs in the HA had a tendency to be slightly higher than the rest of the tumour. However, we observed a differential distribution of cells within the HA, being the density of GAMMs higher at the P region contrasting with GFAP$^+$ cells, which were fewer in this area (Fig. 2 and Supplementary Video 1).
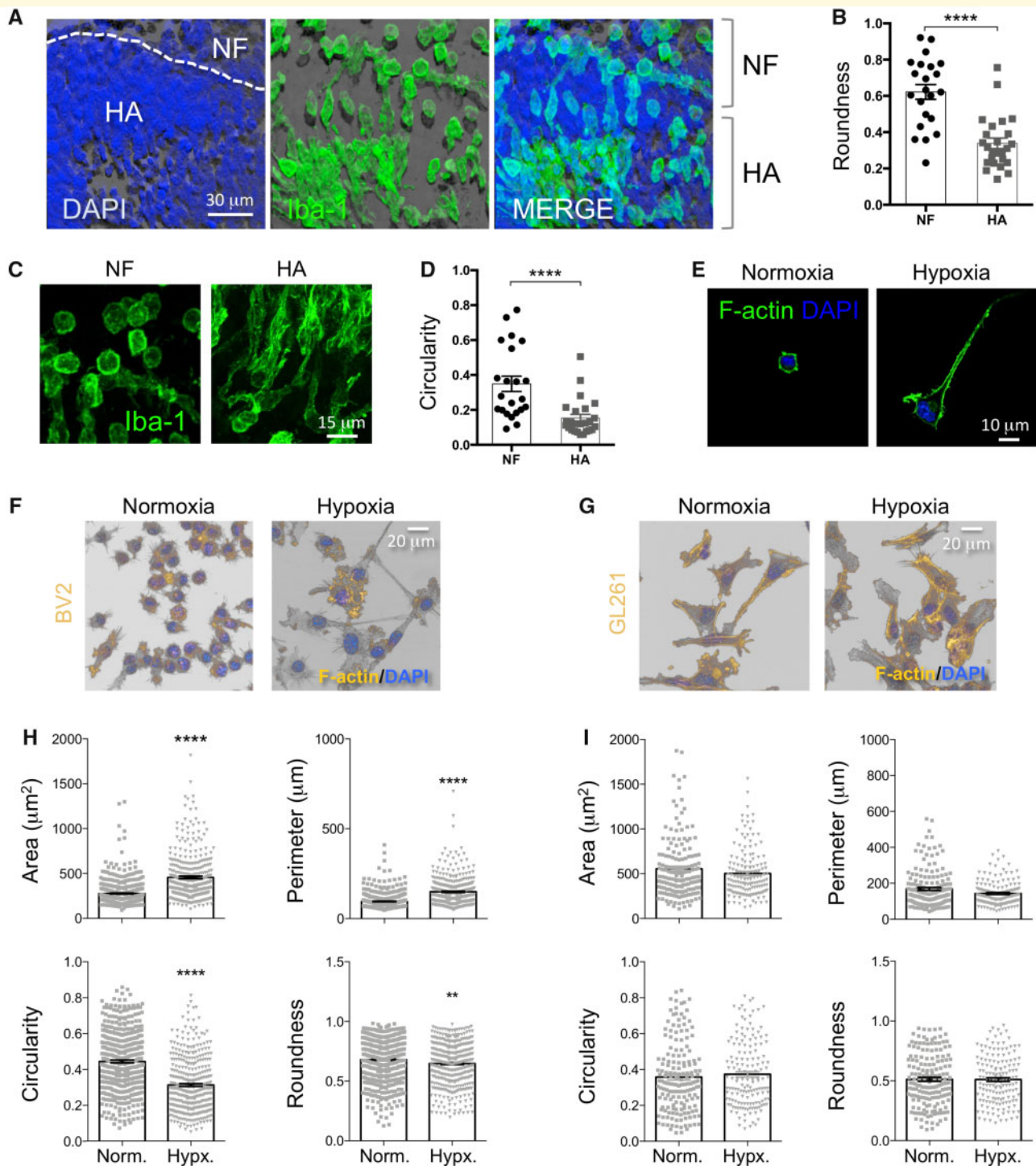
GAMMs become elongated in hypoxic conditions

Since GAMMs at the HA showed elongated morphology differently from an amoeboid morphology found elsewhere (Fig. 3A–D), we hypothesized that this environment,
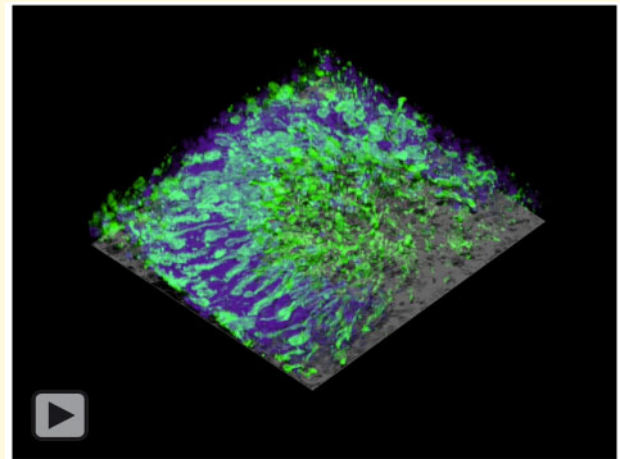

Video 1 The 3D rotation of a human tissue block containing a PP to visualize GAMMs at the HA. A clipping plane is set to facilitate the identification.

essentially characterized by hypoxia (Brat et al., 2004), yet coexistent with hypoglycaemia, may induce this morphological change. Therefore, we set up an *in vitro* experiment with microglial and glioma cell lines to analyse morphometric parameters of the two cell types under these conditions. Our experiments revealed that microglial cells, in contrast with glioma cells, become patently elongated in hypoxic environments suggesting a different motility pattern in these settings, compatible with the palisade-like arrangement (Fig. 3E–I). On the contrary, after hypoglycaemic conditions, although GL261 glioma cells did become elongated, no changes in elongation were seen in microglial cells (Supplementary Fig. 3). Thus, we focused on hypoxic conditions for studying microglial kinetics. In order to know whether elongated morphology coincides with cell motility, we analysed in time-lapse the behaviour of microglia. Importantly, microglial cells in movement adopt a particular shape when travelling, characterized by extended structure, the formation of a protruding leading lamella and a trailing uropod (Fig. 4A–C and Supplementary Video 2). F-actin staining evidenced the actin-rich lamella and the kinetic shape of microglial cells (Fig. 4C–E). Quantification and detailed analyses revealed an apparent increase of kinetic morphology of microglia under hypoxic, in contrast with hypoglycaemic conditions (Fig. 4F and G). Differently, no significant changes were seen in glioma cells (Supplementary Fig. 4A and B). Since the position of the MTOC is potentially oriented towards the leading edge in migrating cells (Nemere et al., 1985; Etienne-Manneville, 2004), we also labelled the MTOC, with γ-Tubulin to analyse its positioning with respect to the leading protrusion (Fig. 4). We observed that the positioning of the MTOC in kinetic microglia (BV2, HAPI and primary microglia) was preferentially located adjacent

Figure 3 Microglia adopt elongated morphology in hypoxic conditions. (**A**) The 3D reconstruction of a human GBM PP containing Iba-1^{+} GAMMs within the palisading HA and NF. (**B**) GAMMs at the HA showed elongated morphology evidenced by a reduction of roundness. (**C**) Detail of morphological differences between Iba-1^{+} cells from NF and HA from human GBM. (**D**) GAMMs show reduced circularity in HA areas when compared with NF. (**E**) BV2 microglial cells show elongated shape under hypoxic conditions. (**F**) Representative confocal images of BV2 cells in normoxia and hypoxia. (**G**) Representative images of glioma cells in normoxia and hypoxia. (**H**) BV2 microglial cells, in contrast with non-myeloid GL261 cells, show an increase in cell area, perimeter and elongated morphology 24 h after hypoxic treatment. (**I**) No significant differences in morphometric parameters were seen in glioma cells.
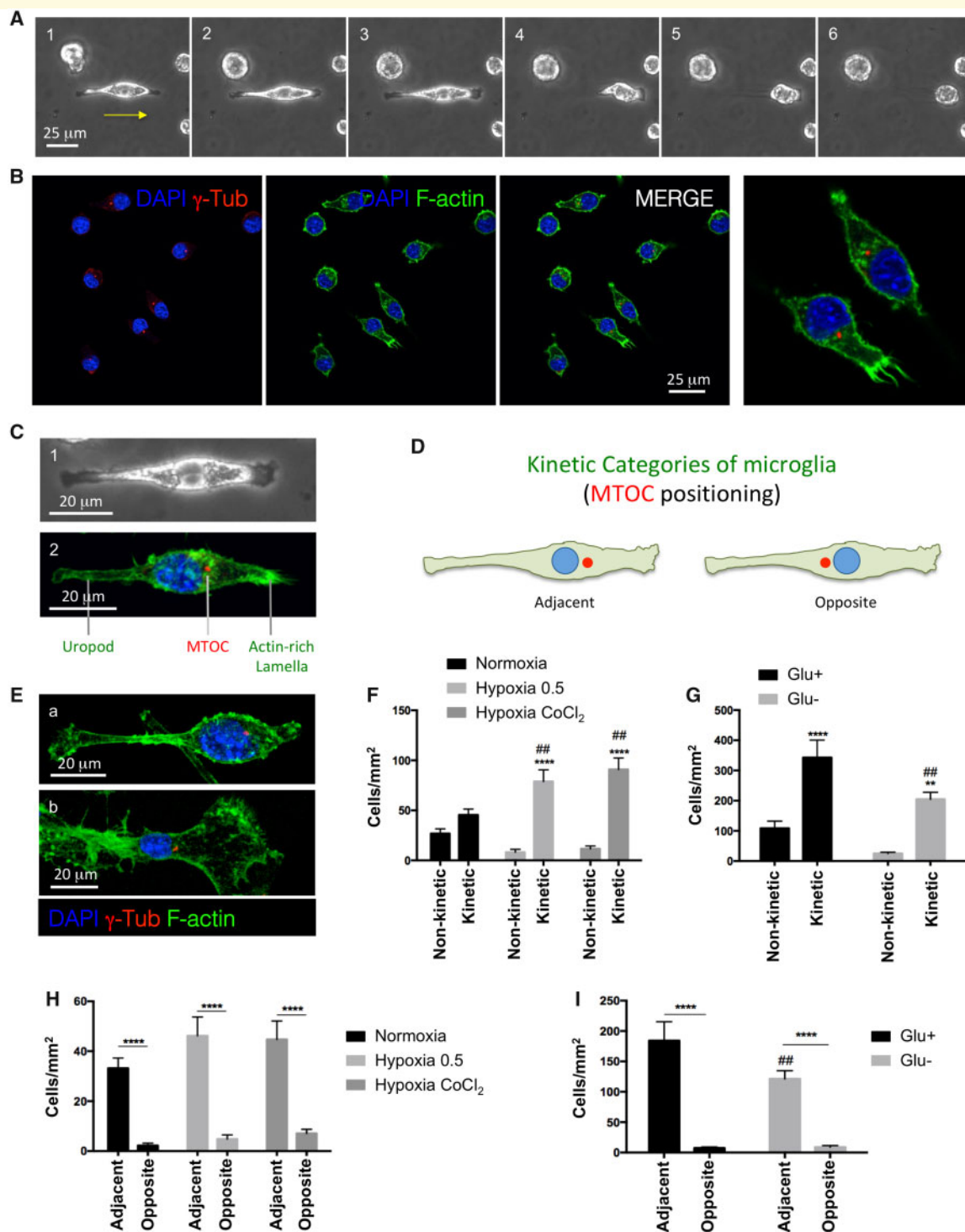
Figure 4 Hypoxia induces oriented kinetic morphology on microglia. (**A**) Time-lapse video reveals the steps that microglial cells undergo when migrating in contrast with neighbouring static cells. (**B**) Confocal analysis of microglial kinetic morphology evidenced by F-actin (green), γ-Tubulin (red) and nuclei counterstained with DAPI (blue). (**C**) (1) BV2 microglial cell in kinetic movement from time-lapse video frame. (2) Maximum intensity projection of BV2 kinetic microglia shows an actin-rich lamella, trailing uropod and γ-Tubulin-rich MTOC. (**D**) Categories of kinetic microglia (adjacent or opposite) according to MTOC position in relation to nucleus and leading lamella. (**E**) HAPI microglial cell line (a) and primary rat microglia (b) show equivalent distribution of the MTOC in relation to the nucleus, protruding lamella and trailing uropod when kinetic. (**F**) Quantification of non-kinetic and kinetic morphology of BV2 microglia in normoxia versus hypoxia. (**G**) Quantification of kinetic and non-kinetic morphology in medium with or without glucose in BV2 microglia. (**H**) Quantification of MTOC position in kinetic-shaped BV2 microglia in normoxia and hypoxia. (**I**) Quantification of MTOC positioning in BV2 microglia with kinetic morphology in glucose-rich medium versus hypoglycaemia. A minimum of 20 cells ($n = 20$) was quantified for each parameter and condition.

to the leading edge in contrast to opposite (back) position (Fig. 4; 95% in BV2, 70% in primary microglia and 65% in HAPI) indicating that the motility of microglial migrating cells encompasses this MTOC positioning. In addition, similar MTOC position was appreciated in kinetic GL261 glioma cells (94%; Supplementary Fig. 4C and D). Importantly, this location was maintained under hypoxic conditions suggesting that the motility and directionality of microglia are run by this centriole position (Fig. 4 and Supplementary Fig. 4).

PP-located GAMMs show preferential cellular orientation according to necrosis location

Knowing the leading MTOC position adopted in kinetic-elongated microglial cells under hypoxic conditions, we analysed in 3D the location of MTOC in GAMMs within the PPs of human GBM samples to establish their preferential orientation. We analysed with high resolution and Z-depth the HA of the PPs separating P, I and D regions, according to the NF position (Fig. 5). We generated specific 3D iso-surfaces and spots in imaging software to locate the orientation of the MTOC (Fig. 5 and Video 2). Our 3D reconstructions show that GAMMs become larger and elongated at the HA, being more prominent at the I area (Fig. 5C–E) and preferentially orienting the MTOC towards the NF at I and D regions (Fig. 5F–G and Video 3), which indicates that GAMMs preferentially migrate to the NF. Interestingly, GAMMs at the P area do not show a preferential directionality suggesting that they may have reached their target location.

Microglia show cellular persistence under hypoxic gradient

Since the directionality of GAMMs at the HA in human PPs is mostly leading towards the NF, we set up an *in vitro* gradient experiment to know whether or not a hypoxic gradient induces changes in microglial migratory behaviour. We observed that hypoxia induces a significant escape of glioma cells towards normoxic media as previously demonstrated by others (Brat *et al.*, 2004; Ayuso *et al.*, 2017), which corroborates the centrifugal characteristics of glioma invasion. In contrast, microglial directionality is not changed either towards normoxia or hypoxia but seems to be affected by the set up gradient (Fig. 6 and Videos 4–7), as cells migrate in a different way. Microglial cells appear clearly elongated and navigate in a straighter manner, defined by the significant increase of the Euclidean distance (Video 5). Thus, microglial cells increase their cellular persistence when exposed to a hypoxic gradient, which explains the elongation at this setting and clarifies the non-centrifugal behaviour towards the NF at the PPs.

GAMMs interact haptotactically with GFAP cells

To further understand the strategy of microglial cells to navigate the HA of the PPs, we analysed the potential interactions of GAMMs with GFAP^{+} cells. We analysed in 3D and high-resolution detail, the combined GFAP/Iba-1 immunofluorescence staining. We observed GFAP^{+} cells displaying a fibrous anisotropic nature at the PPs (Supplementary Fig. 5), in contrast with the isotropy found in other areas, and GAMMs frequently contacting GFAP[+] material at the HA, sharing a similar anisotropic orientation (Fig. 7 and Video 8). These intercellular contacts appeared higher at the I area (Fig. 7), implying the haptotactic travelling of GAMMs through the HA. These intercellular appositions seem to be critical since 100% of GAMMs at the I of the HA were interacting with GFAP fibres (Fig. 7 and Videos 9 and 10). Interestingly, the interactions were established with the tumourigenic GFAP fibres both perpendicular and longitudinal to the NF. Quantifications revealed that longitudinal appositions were significantly longer than the perpendicular ones demonstrating the joined anisotropic orientation of GAMMs and GFAP[+] fibres (Fig. 7 and Video 10). These results imply that GAMMs may utilize the elongated GFAP fibres of the PPs to migrate towards the NF and together with the differential GFAP[+] density along the HA (previously shown in Fig. 2) suggest that haptotaxis could be a crucial strategy of cell motility in this microenvironment.

Microglial phagocytic events increase at the P regions of the HA

Since the haptotactic migration of GAMMs at the PPs is polarized towards the NF, we were wondering about the physiological relevance of reaching this area. Particularly, GAMMs found at the NF of the PPs show a pro-inflammatory phenotype evidenced by MHCII reactivity (Fig. 1), which may indicate an increase of scavenging properties. Thus, to ascertain this, we explored the phagocytic capacity of microglia *in vitro* after classical pro-inflammatory stimulus. We analysed in co-cultures the ability of primary microglia to phagocytose C6 glioma cells after activation with interferon gamma and lipopolysaccharide. Microscopy analysis of this *in vitro* scenario revealed abundant phagocytic events after classic pro-inflammatory activation (Supplementary Fig. 6), verifying the phagocytic competence of microglia towards glioma cells when activated.

Thus, considering the scavenging and phagocytic capacity of GAMMs, we explored and imaged with high resolution the phagocytic events along the PPs. We observed events of GAMMs phagocytosing pyknotic nuclear material or GFAP[+] fragments (Fig. 8). Phagocytic GAMMs, detected by Iba-1 immunolabelling, were identified by having a DAPI[-low]/Iba-1^{+} nucleus, and contained a contiguous Iba-1^{-} space, the phagosome, containing
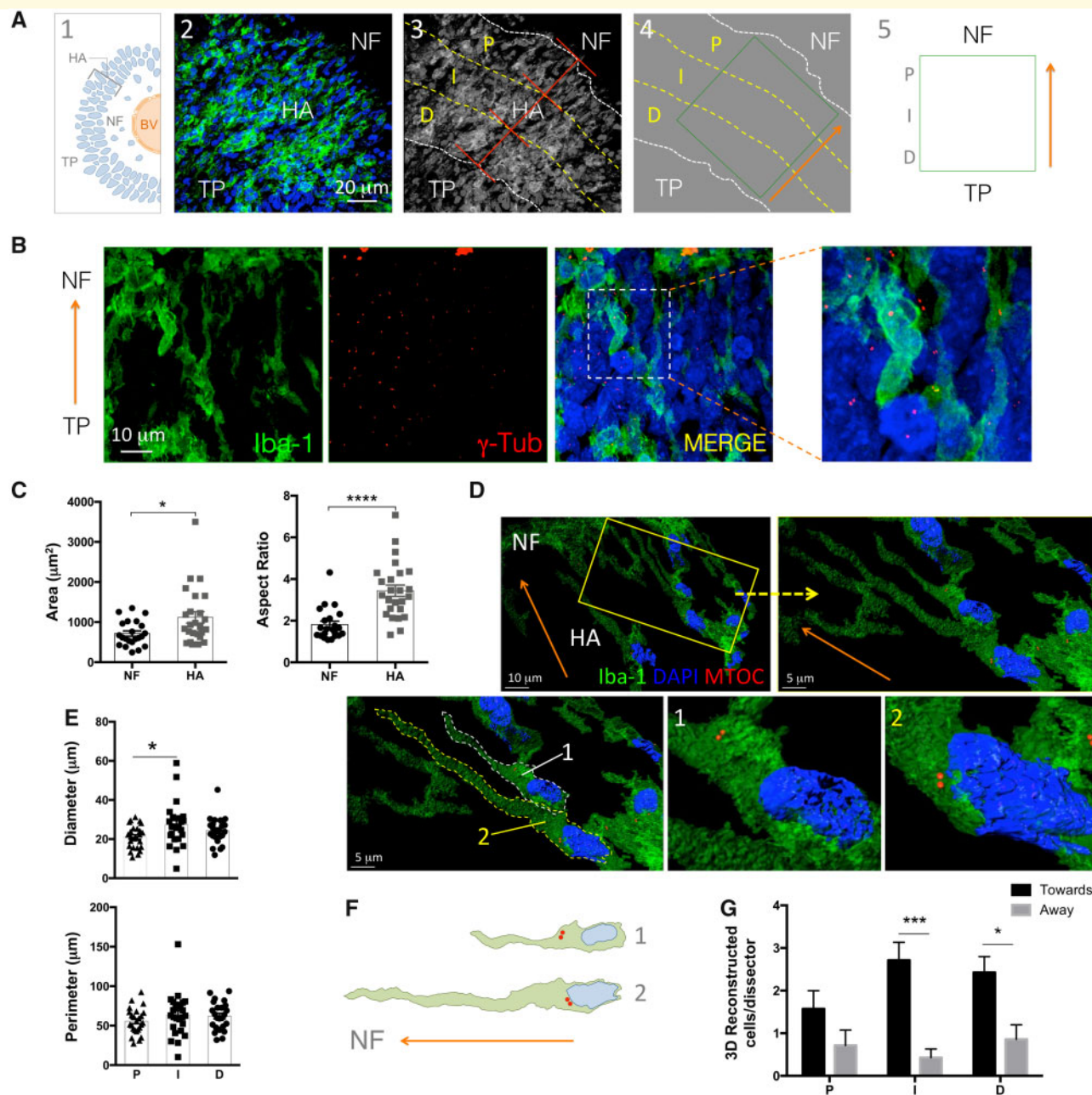
Figure 5 Analysis of GAMMs MTOC position in relation to NF within PPs. Human samples stained for Iba-1 and γ-Tubulin were analysed with 3D high-resolution confocal microscope. We defined the MTOC position towards the NF or TP in proximal (P), intermediate (I) and distal (D) areas. (**A**) (1) Indicative PP diagram for orientation. (2) Confocal image of a representative HA of a necrotic PP between the TP and NF limits. (3) Separation of P, I and D areas in relation to NF proximity. (4) The scanning field at HA was set up rotating the *x* and *y* axes of the system (green square) according to the NF and TP orientation (orange arrow). (5) Images were analysed with these criteria of orientation. (**B**) Representative confocal image of GAMMs labelled with Iba-1 (green), γ-Tubulin (red) and DAPI$^+$ nuclei (blue) within the HA of the PPs. At the higher magnification of the MERGE the MTOC can be identified as γ-Tub accumulations. (**C**) Quantification of the area and aspect ratio of GAMMs in NF and HA. (**D**) Cells could be rendered in 3D to visualize the shape and MTOC position regarding the nucleus and NF location. Representative cells are indicated by 1 and 2. (**E**) Quantification of diameter and perimeter of Iba-1 cells at the PPs show a significant increase of the size at the intermediate area (compatible with elongated shape seen *in vitro*). (**F**) Diagram of representative cells (1 and 2) with prevalent MTOC orientation. (**G**) The quantification of the percentage of cell orientations shows that the majority of cells are oriented towards the NF except in the P area.
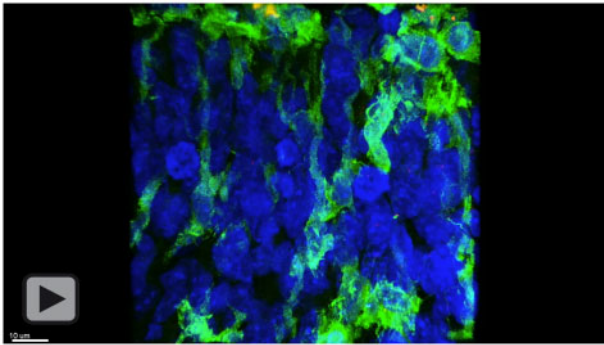
Video 2 Representative 3D processing of the images from human PPs. Original stacks stained for Iba-1, γ-Tubulin and DAPI were treated with the following steps: step 1, Creation of DAPI iso-surface; step 2, detection of MTOC with γ-Tub staining using Imaris Spots; step 3, creation of Iba-1 iso-surface; step 4, filtering of entire cells; and step 5, merging the iso-surfaces and spots to detect cells' orientation.
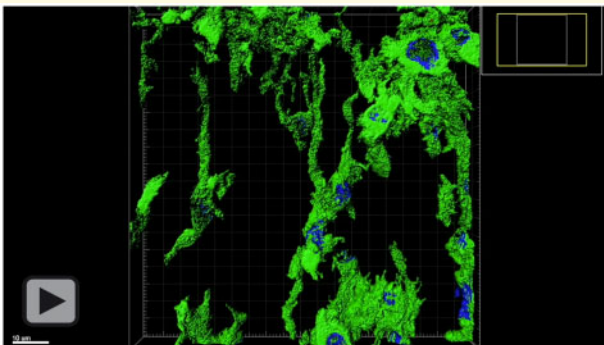
Video 3 Analysis of a processed image to determine the orientation of GAMMs regarding the MTOC position.

DAPI-^{high}/Iba-1^{-} elements, or GFAP^{+} material (Fig. 8 and Video 11). Careful examination of the samples and quantification showed a differential frequency of phagocytic events within the three areas of the HA, being significantly higher at the P area (Fig. 8). These results indicate that GAMMs actively cross the HA of the PPs searching for cellular elements to be engulfed and eliminated.

Discussion

The present study demonstrates that PPs in GBM are populated by a large number of GAMMs that actively migrate towards the NF to phagocytose cellular debris. This migration appears to be taking place in a haptotactic manner, being GFAP^{+} material the substrate and facilitated by the hypoxic gradient.

PP-integrating GAMMs appear elongated at the HA and express CD163, suggesting a skewing of GAMMs to an anti-inflammatory spectrum phenotype at this anatomical compartment. In contrast, GAMMs within the pro-inflammatory spectrum (MHCII^{+}) emerge at the verge of the NF of PPs. These results suggest that GAMMs may switch their phenotypic spectrum, from anti- to pro-inflammatory, when arriving to the P areas. This is consistent with the increase of MHCII (HLA-DR) immunoreactivity at the necrotic border, particularly at the P region of the HA, where GAMMs significantly increase their phagocytic capacity.

By contrast, the anti-inflammatory spectrum appearance is compatible with the migratory behaviour at the I area of the HA. Since CD163 is a receptor that interacts with haemoglobin/haptoglobin complex (Kristiansen *et al.*, 2001; Schaer *et al.*, 2007; Wang *et al.*, 2018), CD163 expression may imply that GAMMs migration towards the NF may be facilitated by the haemorrhage and thrombosis created by the central BV clot. This could result in a haemoglobin/haptoglobin-rich environment in the necrotic areas, product of erythrocyte lysates, that may leak to the HA in a gradient manner.

GAMMs motility in tumours, and particularly in GBM, is not fully understood. In the neoplastic context, the hypoxic environment of PPs influences GAMMs motility in a different way than glioma cells. On the one hand, our cell culture set up demonstrated, as previously reported (Brat *et al.*, 2004), that hypoxia induces the escape of glioma cells towards normoxic conditions, what is congruent with their centrifugal escape in PPs. On the other hand, hypoxic gradient does not induce a chemotactic effect on microglia but importantly induces a straighter migrating behaviour compatible with the higher elongation and their straight directionality found at the human PPs. These results are consistent with the fact that macrophages may be reprogrammed under hypoxic conditions, having a tendency to present an anti-inflammatory spectrum phenotype (Raggi *et al.*, 2017), being hypoxia a trigger of migration and the transition to an alternative spectrum (Leblond *et al.*, 2016).

Besides the effect of hypoxia, our study also reflects that GAMMs may use a haptotactic strategy to navigate the HA of the PP. This strategy is not rare in tumour microenvironments, and specific physical changes as the fibrillary disposition, may directly intervene in the invasion process (Oudin and Weaver, 2016). Interestingly, mathematical models also show that haptotaxis could be the connection between cell locomotion and the resulting persistent walk behaviour on long-time scales (Dickinson, 2000). Thus, tissue fibres can serve as a haptotactic cue. As tumour cells enhance their efficiency of migration restricting protrusions along aligned fibres such as collagen (Riching *et al.*, 2014), in our scenario, the fibrillary nature of GFAP^{+} cells at the HA may also facilitate the persistent motility of GAMMs within the PPs. This is consistent with the elongation and focalization of the GAMMs' protrusions and the variation of GFAP^{+} density along the HA.
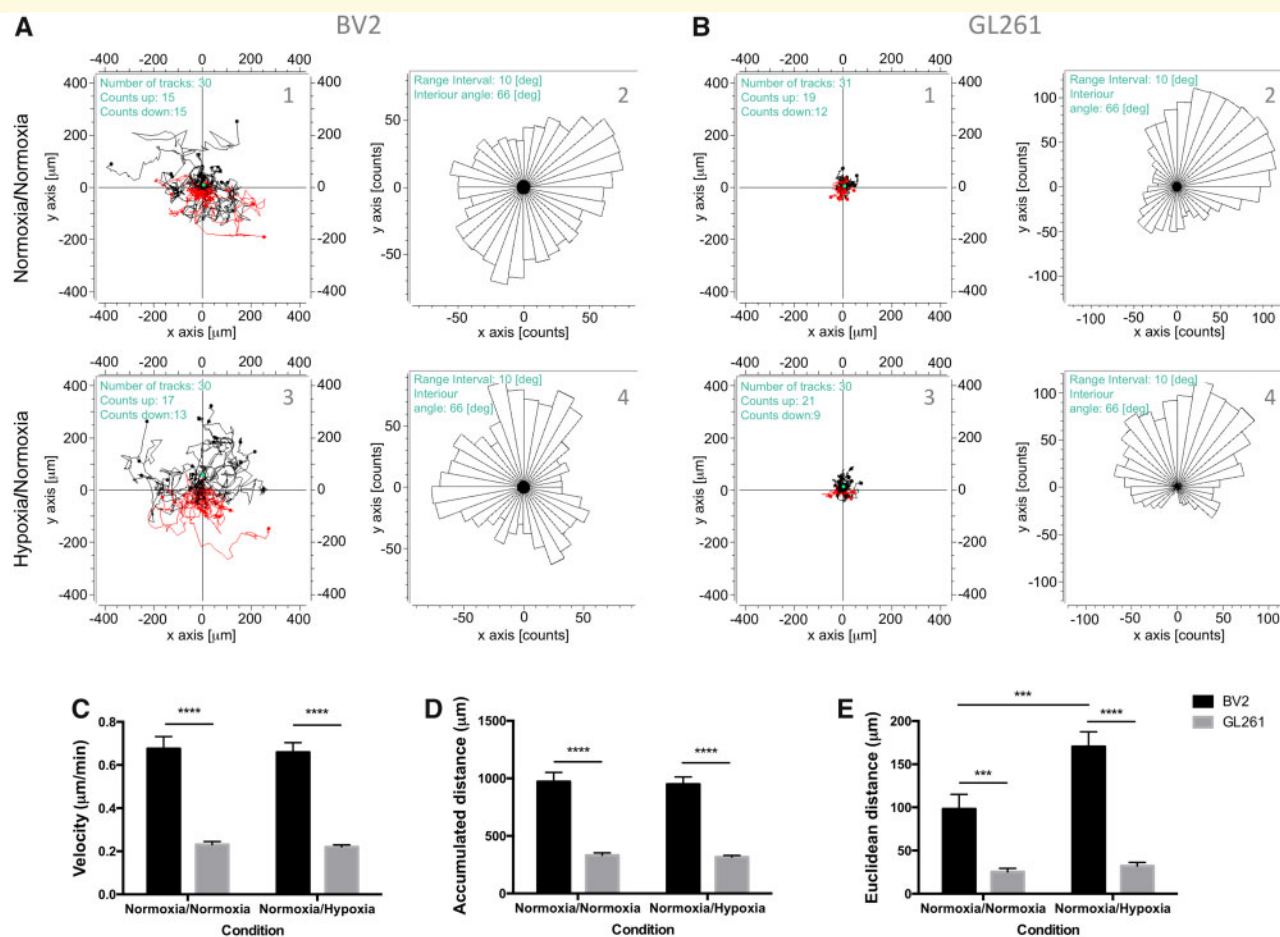
Figure 6 Microglial cells do not escape from hypoxia and navigate straightly. (**A**) Microglia behave similarly when exposed 24 h to normoxic (representative cell trajectories in plot graph 1 and distribution of migrating angles in rose graph 2) and hypoxic conditions (analogous representation of cell tracks in 3 and rose graphs in 4). Black tracks are cells ending in the upper quadrant while red tracks are cells ending in the lower quadrant. (**B**) Glioma cells migrate away from hypoxic conditions. When comparing the exposure to normoxic media (1 and 2) and hypoxic gradient (3 and 4) during 24 h, glioma cells move away from the hypoxic source. Green dots in the graphs (1 and 3) represent the centre of mass. Rayleigh test for directionality revealed a significant directionality only for glioma GL261 cells [$P < 0.01$ ($P = 0.00282$)] in a hypoxic gradient towards normoxia in contrast with no gradient ($P > 0.05$) and microglia BV2 cells ($P > 0.05$ with and without gradient). In all cases, microglia show higher motility, migrating with higher velocity (**C**) and travel longer distances (**D**) than glioma cells. (**E**) Although hypoxia–normoxia gradient does not modify the velocity and accumulated distance, microglia show higher Euclidean distance, meaning that they migrate straighter in these conditions. The tracks of 30 cells ($n = 30$) were quantified for each parameter and condition.

The advantageous effect for tumour expansion of GAMMs recruitment at the PPs is to be understood, but it could be related with the generation of new BVs and debris clearance. In fact, it has been demonstrated that tumour-associated macrophages promote angiogenesis in tumours and specifically in glioma (Chen *et al.*, 2014). Thus, our results suggest that particularly the migration of anti-inflammatory GAMMs to these thrombotic areas may induce vasculogenesis in this environment, facilitating the development of the tumours. Previous studies in other neoplastic scenarios, such as experimental models of breast cancer, have shown that anti-inflammatory skewed macrophages migrate to avascular hypoxic areas promoting tumour progression by stimulating

angiogenesis (Casazza *et al.*, 2013), highlighting the relevance of the microenvironment to determine pro-tumoural activity (Rivera and Bergers, 2013). Furthermore, the haemoglobin-haptoglobin receptor CD163 may indeed play a critical role in this particular process. Recently, although in a different clinical scenario, it has been found that haemoglobin-haptoglobin-induced CD163 signalling in macrophages promotes the production and release of angiogenic factors (Guo *et al.*, 2018). Coherently, the expression of CD163$^+$ by microglia-macrophages populating PPs suggests their putative angiogenic properties to stimulate GBM growth within this microenvironment.

We also show that, while tumour cells escape from the hypoxic core, GAMMs travel through the HA towards
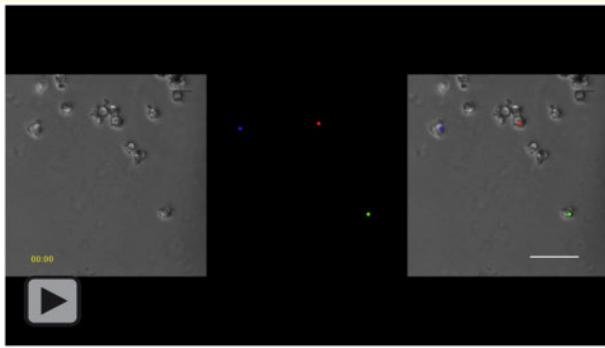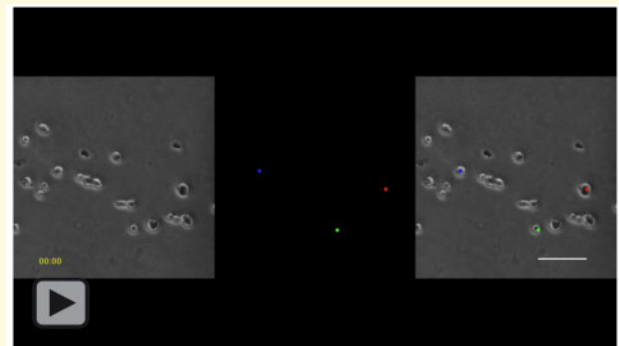
Video 4 Microglial cells present a rapid random walk when exposed to normoxic conditions. A 24-h time-lapse is shown on the left panel. The track of three representative cells is displayed in the central panel. A merge of the two panels is shown on the right.
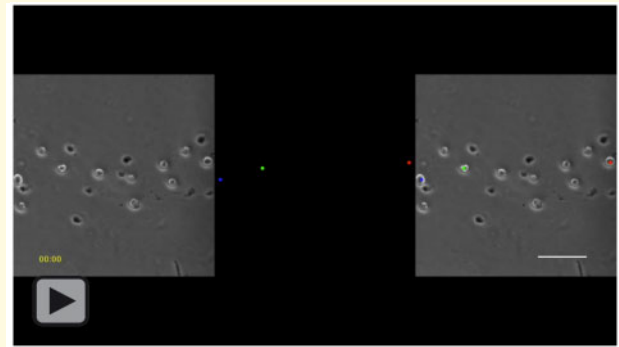
Video 6 Glioma cells present a slow random walk when exposed to normoxic conditions. A 24-h time-lapse is shown on the left panel. The track of three representative cells is displayed in the central panel. A merge of the two panels is shown on the right.
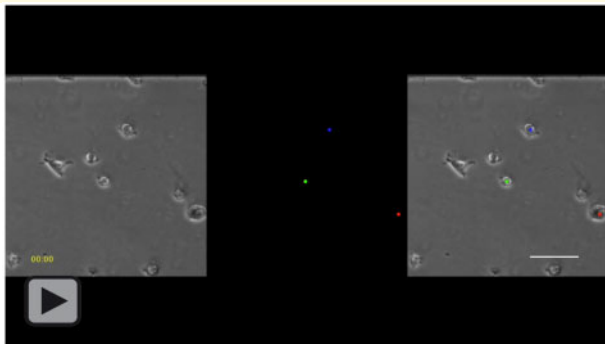

Video 5 Microglial cells present cellular persistence when exposed to hypoxic gradient. A 24-h time-lapse is shown on the left panel. The track of three representative cells is displayed in the central panel. A merge of the two panels is shown on the right.

Video 7 Glioma cells slowly escape the hypoxic environment when exposed to hypoxic gradient. A 24-h time-lapse is shown on the left panel. The track of three representative cells is displayed in the central panel. A merge of the two panels is shown on the right.

the NF to phagocytose, probably repairing and containing the adverse environment. This may also be an important process of the development of the PPs, paradoxically contributing to the tumour expansion. Apoptotic cells at the necrosis may be a strong attracting signal for phagocytes to this site (Cullen *et al.*, 2013; Elliott and Ravichandran, 2016). While apparently the phagocytic capacity of GAMMs may serve in favour of tumour clearance, the focus on phagocytosis of apoptotic corpses may as well divert microglia macrophages from eliminating tumour cells (Reiter *et al.*, 1999). In PPs, the location is especially critical because the phagocytic capacity is limited to the P areas towards the NF, which represents the opposite direction of the tumour expansion. As a result, corpse clearance and repair at the NF can also be essential for preparing the tissue for new neoplastic invasion or, as mentioned above, the establishment of new vasculature.

Tumour infiltrated macrophages/microglia play a supportive role of GBM (Zhou *et al.*, 2015); thus, it is critical to understand their behaviour within the different microenvironments of the tumour and how interplay with the growth of the tumour mass occurs. Particularly for PPs, since they are distinguishable pathological hallmarks of the malignancy of GBMs, the role of GAMMs in this scenario becomes relevant for the progression of the tumour, and therefore, should be considered as an important niche for therapeutic intervention. We suggest that GAMMs in PPs may be a critical factor for tumour development in this microenvironment since they repair the vaso-occlusive and prothrombotic ecosystem of the NF that may contribute to accelerate tumour mass growth and invasion. Alternatively, since the phagocytic capacity of GAMMs persists in GBM, new therapeutic approaches should be oriented towards the re-programming of these cells towards the phagocytosis and clearance of malignant cells in the TP.
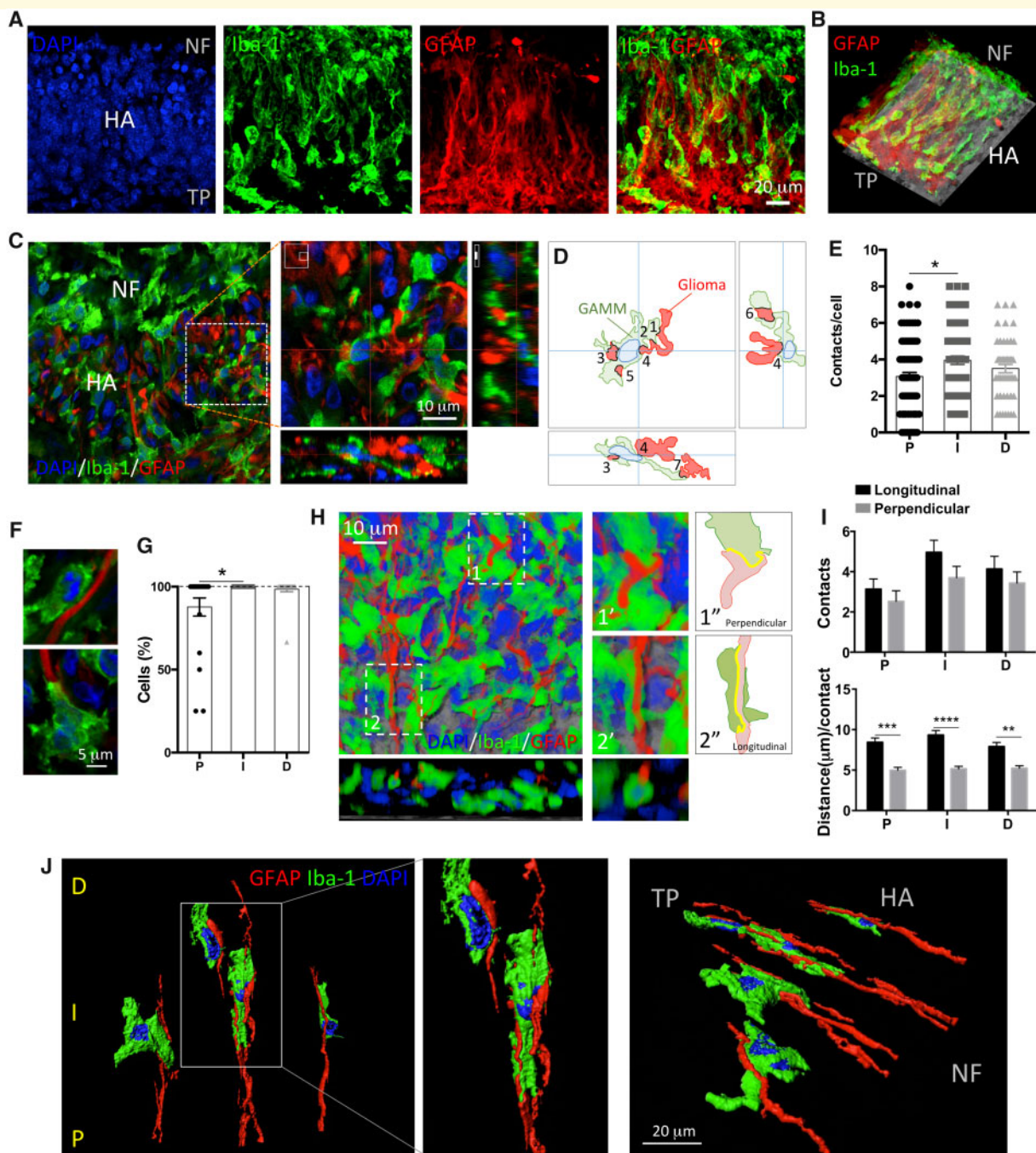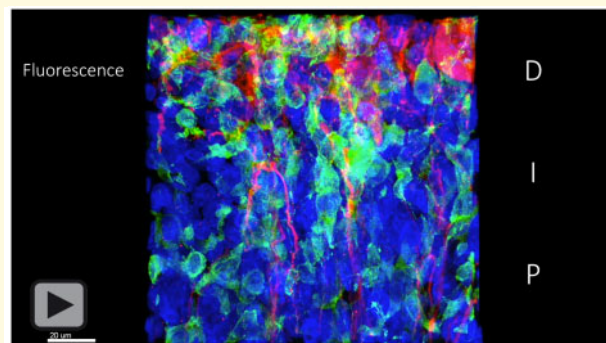
Figure 7 Haptotactic interaction of GAMMs with GFAP⁺ fibres at the human PPs. (**A**) Representative PP by confocal scanning the nuclei (DAPI), GAMMs (Iba-1) and glioma cells (GFAP) at the HA limited by the NF and TP. (**B**) The 3D reconstruction of the image shown in A. (**C**) Confocal visualization of GAMMs at the HA near the NF limit. Higher magnification of broken white line square is displayed to the right to show GAMMs interacting with GFAP⁺ fibrils, also shown in different optical planes and indicated in orthogonal views at the Z planes. (**D**) Diagram representing the analysis of Iba-1-GFAP interactions based on C including the orthogonal views. (**E**) Quantification of the number of interactions with GFAP per Iba-1⁺ cell at the P, I and D areas. The number of contacts is significantly increased at the I area. (**F**) Representative Iba-1 cells interacting with fibrous GFAP cells at the PPs. (**G**) Quantification of the percentage of Iba-1 cells establishing contacts with GFAP cells at the HA of the PP. (**H**) The 3D reconstruction of Iba-1 and GFAP interactions at the HA. Representative perpendicular (1) and longitudinal (2) interactions are indicated in white broken-line squares, which are shown in higher magnifications in 1′ and 2′. Orthogonal view at the level of the longitudinal interaction is shown. Illustrations of perpendicular and longitudinal interactions are shown in 1″ and 2″. (**I**) Quantification of the number and distance of longitudinal and perpendicular contacts at the P, I and D areas. (**J**) The 3D reconstruction of GAMMs within the HA of a human PP in apposition to GFAP fibrils. Zoom from white rectangle is shown. Oblique view is shown in image on the right.
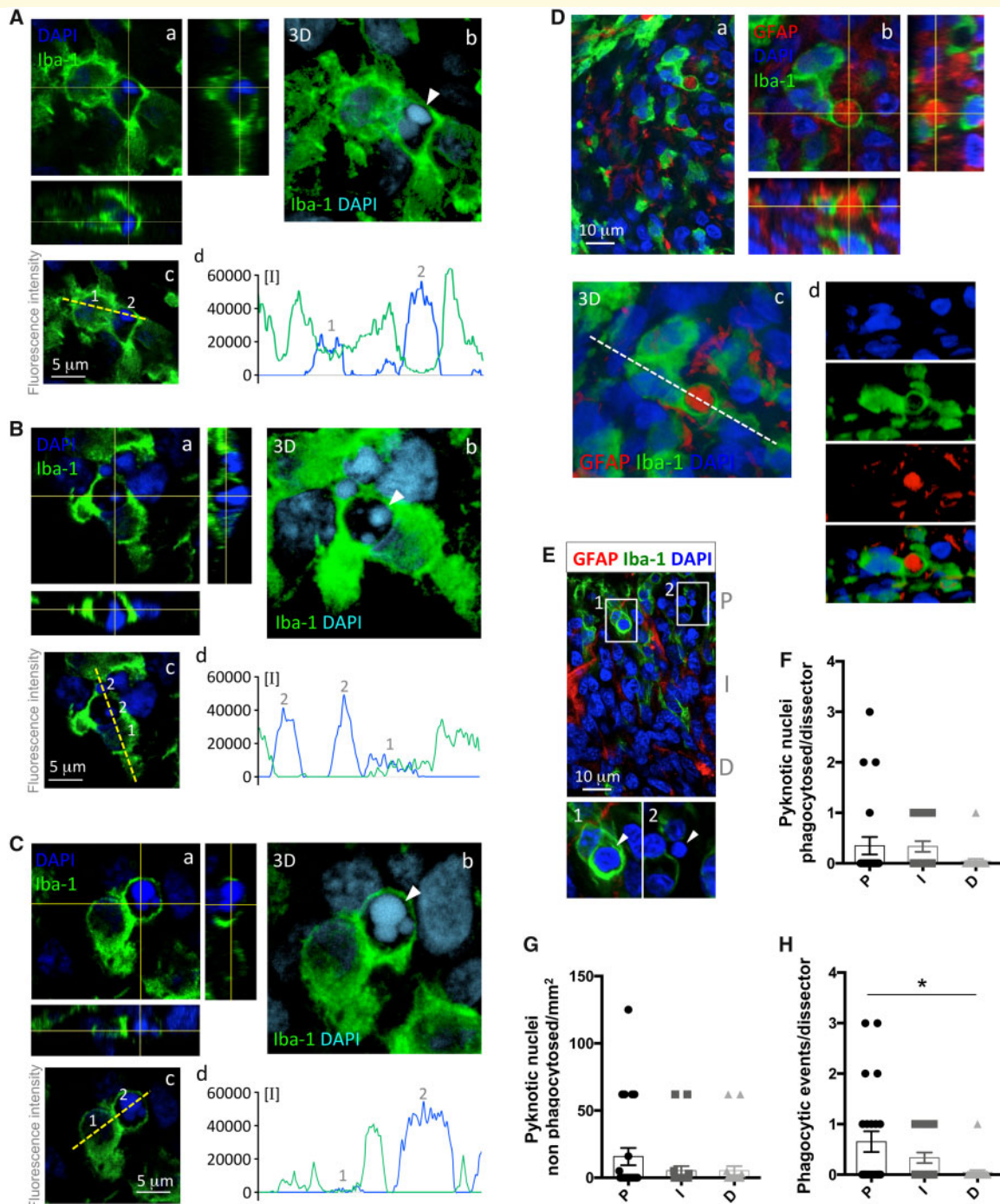
Figure 8 Increased phagocytic capacity of GAMMs at the NF proximity. (**A**) Engulfing GAMMs at the human PPs evidenced with Iba-1 and DAPI stainings. Nuclei with pyknotic characteristics could be seen in Iba-1⁻ space within GAMM. Orthogonal views evidenced the engulfing along the z-stack (**a**). The 3D reconstruction at central clipping plane shows the phagosome containing pyknotic nuclei (arrowhead) surrounded by Iba-1 (**b**). Analysis of relative fluorescence intensity was measured along yellow broken line (**c**). Plot profile from **c** is shown in **d**. Nuclei (normal, 1 and pyknotic, 2) are also indicated in the profile plot (**d**). Analogous examples of phagocytosis are shown in **B** and **C** (in plot profiles 1 is for regular nucleus and 2 for pyknotic nuclei). (**D**) Phagocytosis of GFAP⁺ material at the human PPs. Confocal overview of the HA stained for Iba-1, GFAP and DAPI (**a**). Detail of a phagocytic event from the P region of the HA and orthogonal views at the indicated planes (**b**). The 3D visualization at central clipping plane showing GFAP⁺ material at the phagosome (**c**). Lateral view of the phagocytic event from clipping plane shown in **c** with white broken line (**d**). (**E**) Example of a HA of a PP indicating the P, I and D areas. Pyknotic nuclei can be detected phagocytosed (1) or isolated (2), especially at the P and I regions. (**F**) Quantification of phagocytosed nuclei in P, I and D. (**G**) Quantification of isolated pyknotic nuclei in P, I and D. (**H**) Estimation of the frequency of phagocytic events in P, I and D.
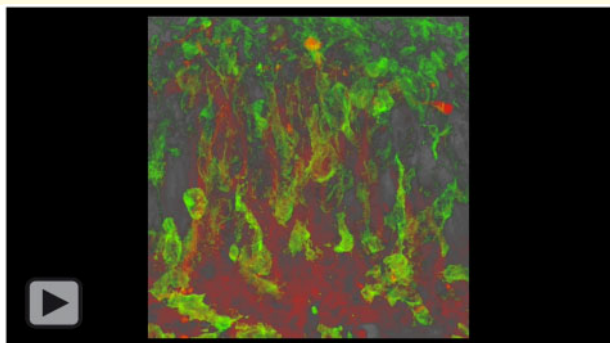
Video 8 Rotation of a 3D tissue transparency to show the anisotropy of the PP shared by GAMMs (Iba-1), and malignant glioma cells and remnant astrocytes (GFAP) across the HA.

Video 10 The 3D reconstruction of a representative HA of a human PP. Iso-surfaces of Iba-1, GFAP and DAPI revealed the haptotactic interactions of GAMMs with fibrils.
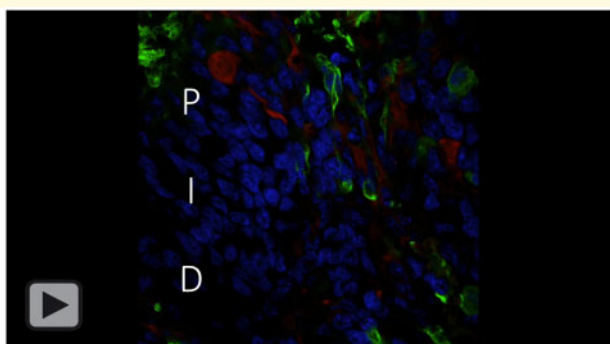
Video 9 Confocal Z-scan at the HA area of a PP including P, I and D regions. Interactions of GAMMs (Iba-1) and malignant cells and remaining reactive astrocytes (GFAP) can be especially seen at the I region. Phagocytic events can be observed at the P area.
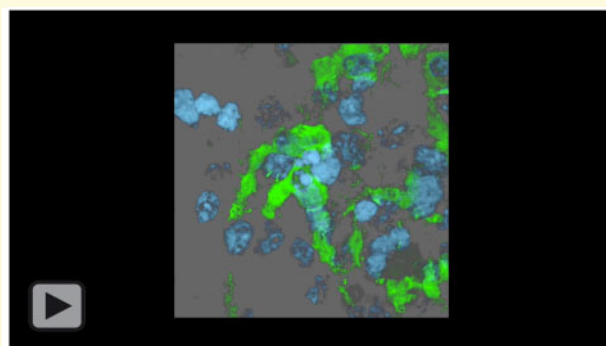
Video 11 Visualization of a phagocytic event at the P region of a human PP. The 3D reconstruction of a confocal image shows an Iba-1+ cell engulfing DAPI+ pyknotic material.

Supplementary material

Supplementary material is available at *Brain Communications* online.

Acknowledgements

This work is dedicated to the loving memory of Carlos Barcia Mariño (1941–2014), Head of the Department of Neurosurgery, Valencia General Hospital. We would like to thank all the supporting institutions, which are listed in the funding section. We also acknowledge the contribution of the National Cancer Institute for contributing with Research Material (GL261 Cells, NCI MTA#1-4638-14). We would also like to thank all the personnel from the Administration and Technical Laboratories of the *Institut de Neurociències*, for the help provided at the *Universitat Autònoma de Barcelona*, very especially to the excellent technicians at the Microscopy Core, Núria Barba and Saioa Mendizuri and the Cell Culture Unit, Cristina Gutierrez and Antonio Cambero.

Competing interests

The authors report no competing interests.

References

Ayuso JM, Monge R, Martinez-Gonzalez A, Virumbrales-Munoz M, Llamazares GA, Berganzo J, et al. Glioblastoma on a microfluidic chip: generating pseudopalisades and enhancing aggressiveness through blood vessel obstruction events. Neuro-Oncology 2017; 19: 503–13.

Brat DJ, Castellano-Sanchez AA, Hunter SB, Pecot M, Cohen C, Hammond EH, et al. Pseudopalisades in glioblastoma are hypoxic, express extracellular matrix proteases, and are formed by an actively migrating cell population. Cancer Res 2004; 64: 920–7.

Brat DJ, Van Meir EG. Vaso-occlusive and prothrombotic mechanisms associated with tumor hypoxia, necrosis, and accelerated growth in glioblastoma. Lab Invest 2004; 84: 397–405.

Casazza A, Laoui D, Wenes M, Rizzolio S, Bassani N, Mambretti M, et al. Impeding macrophage entry into hypoxic tumor areas by Sema3A/Nrp1 signaling blockade inhibits angiogenesis and restores antitumor immunity. Cancer Cell 2013; 24: 695–709.

Chen X, Zhang L, Zhang IY, Liang J, Wang H, Ouyang M, et al. RAGE expression in tumor-associated macrophages promotes angiogenesis in glioma. Cancer Res 2014; 74: 7285–97.

Cullen SP, Henry CM, Kearney CJ, Logue SE, Feoktistova M, Tynan GA, et al. Fas/CD95-induced chemokines can serve as "find-me" signals for apoptotic cells. Mol Cell 2013; 49: 1034–48.

Diaz LR, Saavedra-Lopez E, Romarate L, Mitxitorena I, Casanova PV, Cribaro GP, et al. Imbalance of immunological synapse-kinapse states reflects tumor escape to immunity in glioblastoma. JCI Insight 2018; 3: e120757.

Dickinson RB. A generalized transport model for biased cell migration in an anisotropic environment. J Math Biol 2000; 40: 97–135.

Elliott MR, Ravichandran KS. The dynamics of apoptotic cell clearance. Dev Cell 2016; 38: 147–60.

Etienne-Manneville S. Cdc42–the centre of polarity. J Cell Sci 2004; 117: 1291–300.

Guo L, Akahori H, Harari E, Smith SL, Polavarapu R, Karmali V, et al. CD163+ macrophages promote angiogenesis and vascular permeability accompanied by inflammation in atherosclerosis. J Clin Invest 2018; 128: 1106–24.

Hambardzumyan D, Gutmann DH, Kettenmann H. The role of microglia and macrophages in glioma maintenance and progression. Nat Neurosci 2016; 19: 20–7.

Kristiansen M, Graversen JH, Jacobsen C, Sonne O, Hoffman HJ, Law SK, et al. Identification of the haemoglobin scavenger receptor. Nature 2001; 409: 198–201.

Leblond MM, Gerault AN, Corroyer-Dulmont A, MacKenzie ET, Petit E, Bernaudin M, et al. Hypoxia induces macrophage polarization and re-education toward an M2 phenotype in U87 and U251 glioblastoma models. Oncoimmunology 2016; 5: e1056442.

Nemere I, Kupfer A, Singer SJ. Reorientation of the Golgi apparatus and the microtubule-organizing center inside macrophages subjected to a chemotactic gradient. Cell Motil 1985; 5: 17–29.

Oudin MJ, Weaver VM. Physical and chemical gradients in the tumor microenvironment regulate tumor cell invasion, migration, and metastasis. Cold Spring Harb Symp Quant Biol 2016; 81: 189–205.

Poon CC, Sarkar S, Yong VW, Kelly J. Glioblastoma-associated microglia and macrophages: targets for therapies to improve prognosis. Brain 2017; 140: 1548–60.

Raggi F, Pelassa S, Pierobon D, Penco F, Gattorno M, Novelli F, et al. Regulation of human macrophage M1-M2 polarization balance by hypoxia and the triggering receptor expressed on myeloid cells-1. Front Immunol 2017; 8: 1097.

Reiter I, Krammer B, Schwamberger G. Cutting edge: differential effect of apoptotic versus necrotic tumor cells on macrophage antitumor activities. J Immunol 1999; 163: 1730–2.

Riching KM, Cox BL, Salick MR, Pehlke C, Riching AS, Ponik SM, et al. 3D collagen alignment limits protrusions to enhance breast cancer cell persistence. Biophys J 2014; 107: 2546–58.

Rivera LB, Bergers G. Location, location, location: macrophage positioning within tumors determines pro- or antitumor activity. Cancer Cell 2013; 24: 687–9.

Rong Y, Durden DL, Van Meir EG, Brat DJ. 'Pseudopalisading' necrosis in glioblastoma: a familiar morphologic feature that links vascular pathology, hypoxia, and angiogenesis. J Neuropathol Exp Neurol 2006; 65: 529–39.

Schaer DJ, Alayash AI, Buehler PW. Gating the radical hemoglobin to macrophages: the anti-inflammatory role of CD163, a scavenger receptor. Antioxid Redox Signal 2007; 9: 991–9.

Wang G, Wang L, Sun XG, Tang J. Haematoma scavenging in intracerebral haemorrhage: from mechanisms to the clinic. J Cell Mol Med 2018; 22: 768–77.

Wippold FJ 2nd, Lammle M, Anatelli F, Lennerz J, Perry A. Neuropathology for the neuroradiologist: palisades and pseudopalisades. AJNR Am J Neuroradiol 2006; 27: 2037–41.

Zhou W, Ke SQ, Huang Z, Flavahan W, Fang X, Paul J, et al. Periostin secreted by glioblastoma stem cells recruits M2 tumour-associated macrophages and promotes malignant growth. Nat Cell Biol 2015; 17: 170–82.